1 **Direct precipitation of siderite in ferruginous environments**

2

3 Ashley Grengs[1,2*], Gabrielle Ledesma[3,4], Yijun Xiong[5], Sergei Katsev[6, 7], Simon W. Poulton[5],

4 Elizabeth D. Swanner[4], Chad Wittkop[2]

5

6 [1] *Earth Science Department, University of New Hampshire, 305 James Hall, Durham, NH 03824*

7 [2] *Department of Biochemistry, Chemistry, and Geology, Minnesota State University, 241 Ford*

8 *Hall, Mankato, MN 56001*

9 [3] *Memorial University of Newfoundland, St. John's NLA1C 5S7, Canada*

10 [4] *Department of Geological and Atmospheric Sciences, Iowa State University, 2337 Osborn*

11 *Drive, Ames, IA, 50011*

12 [5] *School of Earth and Environment, University of Leeds, Leeds LS2 9JT, UK*

13 [6] *Large Lakes Observatory, University of Minnesota Duluth 2205 East 5th Street, Duluth, MN*

14 *55812*

15 [7] *Department of Physics and Astronomy, University of Minnesota Duluth, 1049 University Drive,*

16 *Duluth, MN 55812*

17

18 **ABSTRACT**

19 Siderite ($FeCO_3$) is often assumed to precipitate from dissimaltory reduction of Fe-

20 (oxyhydr)oxides, but geochemical and mineralogical analyses from ferruginous (anoxic, Fe-rich)

21 Canyon Lake, USA suggest Fe-carbonate represents a direct early precipitate unrelated to

22 substantial oxide burial. X-ray absorption near edge structure (XANES) spectroscopy of

23 sediment trap materials and an anoxic sediment core indicated a mixture of Fe(II) and Fe(III) in

24 water column particulates and ferruginous surface sediments, while all Mn phases were reduced.

25 About 60 cm below the sediment-water interface, Fe-Mn carbonates were detected by X-ray

26 diffraction and XANES, while Fe extended X-ray absorption fine structure (EXAFS) spectra

27 were best fit with combinations of a biogenic Fe-oxyhydroxide ("Bio Fe"), greigite, and siderite.

28 Sediment Fe speciation indicates a large pool of reduced Fe with a minor component of oxides.

29 Although we found no evidence of significant carbonate phases above or below the 60 cm

30 horizon, equilibrium modelling indicates siderite supersaturation throughout surface sediment

31 porewater, with pH as the primary control on supersaturation. We conclude that delivery of

32 wildfire ash to sediments increased pH, initiating siderite precipitation from ferruginous

33 porewater.

34

35 **INTRODUCTION**

36 Siderite ($FeCO_3$) occurs in sediments throughout Earth's history (Ohmoto *et al.,* 2004), and is a

37 common component in Precambrian iron formations (Ifs; Konhauser *et al.,* 2017). Despite the

38 diversity of environments in which siderite occurs, two mechanisms are generally considered to

39 drive its formation: 1) direct precipitation from an anoxic and iron-enriched (ferruginous) fluid;

40 and 2) as a diagenetic product derived from reduction of primary iron (oxyhydr)oxides coupled

41 to microbial organic carbon remineralization (Heimann *et al.,* 2010;). While dissimilatory

42 reduction of reactive iron (oxyhydr)oxides such as ferrihydrite may explain the negative C-

43 isotopic composition and textures of many lacustrine siderite occurrences (Vuillemin *et al.,*

44 2019), the textures and C-isotope signatures of well-preserved Precambrian IFs are also

45 consistent with precipitation from ferruginous seawater (Beukes *et al.,* 1990; Siahi *et al.,* 2020;

46 Riding *et al.,* 2022), perhaps under a strong hydrothermal influence (Jiang and Tosca, 2019).

47

48   To constrain the conditions that govern natural siderite precipitation, we examined iron (Fe) and

49   manganese (Mn) phases in water column particulates and recent sediments from ferruginous

50   Canyon Lake (CL) in Michigan, USA. Modern ferruginous lakes serve as analogue systems

51   informing our understanding of biogeochemical dynamics in anoxic Precambrian oceans

52   (Swanner *et al.,* 2020). Canyon Lake is an ideal site to investigate these processes, as its

53   ferruginous bottom waters are poised near siderite supersaturation, and its water column has been

54   chemically stable for at least the last 80 years (Lambrecht *et al.,* 2018). Found in a boreal shield

55   setting, groundwater supplies the small CL basin with dissolved iron, and its water column

56   chemistry and methane cycling embed processes similar to those thought to have dominated

57   Precambrian oceans (Lambrecht *et al.,* 2020).

58

59   **METHODS**

60   Multiparameter sondes were used to determine CL water column properties in 2018 and 2019,

61   and water samples for cation and anion analysis were collected in May 2018 following standard

62   procedures. A sediment freeze core was collected in February 2018, and sediment traps were

63   deployed in 2019. Samples for iron speciation, XANES, and EXAFS were collected processed

64   under an N_2 atmosphere and stored anoxically until analysis. See Supplementary Information

65   (SI) for Site Description, Methods, and full Results.

66

67   **RESULTS AND DISCUSSION**

68

69   **Iron and Manganese Phases in Ferruginous Waters**

70 Centroid energies for Fe XANES pre-edge peaks from sediment trap material from 7.5, 15 and

71 20 m were ~7114 eV (Fig. 1; Fig. S-3), consistent with a mixture of Fe(II) and Fe(III). Best fits

72 from linear combination fitting of Fe extended X-ray absorption fine structure (EXAFS) spectra

73 for the sediment trap samples included, in order of contribution to fits, a biogenic Fe-

74 oxyhydroxide ("Bio Fe"; Toner *et al.,* 2009), siderite, magnetite (Hansel *et al.,* 2005), green rust,

75 and greigite. However, the quality of these fits was low, likely due to the limited amount of

76 sample producing spectra with low signal to noise, or the presence of poorly crystalline phases.

77 The main Mn K-edge peak energy in sediment trap samples (~6552 eV) was consistent with

78 Mn(II) rather than Mn(III) or Mn(IV) (~6558 eV), indicating that Mn-oxides are not present in

79 the water column (Fig. 1).

80

81 **Figure 1** Geochemical and mineralogical characteristics of water column solutes and solid

82 phases. **(a)** Dissolved solutes in the CL water column. The oxycline (decrease in dissolved

83 oxygen) occurs between 7-12 m, and the chemocline (increase in dissolved Fe) occurs between

84 17-19 m. Sediment traps were deployed at 7.5, 15 and 22 m. **(b)** Sediment trap Fe XANES

85 analyses. Pre-edge centroid energies are ~7114 eV, consistent with a mixture of Fe(II) and

86 Fe(III). **(c)** Sediment trap Mn K-edge XANES analyses. Peaks have lower energy (~6552 eV)

87 compared to Mn-oxides (~6558 eV), consistent with Mn(II) minerals.

88

89 **Sediment Geochemistry and Mineralogy**

90 The sediments contain a large pool of highly reactive Fe (Fe_{HR}; average 3.59 ± 0.52 wt. %), with

91 the Fe_{HR} pool dominated by unsulfidized Fe(II) phases ($Fe(II)_{unsulf}$), with a generally low

92 concentration of poorly crystalline ferric (oxyhydr)oxide phases such as ferrihydrite (Fe_{ox1}). The

93   remaining Fe phases, comprising crystalline Fe (oxyhydr)oxides (Fe_{ox2}), magnetite (Fe_{mag}) and

94   pyrite (Fe_{py}), were less significant throughout the core (Fig. 2; Table S-1).

95

96   Calculations using porewater DIC and the solute chemistry of the deepest CL waters show

97   siderite to be supersaturated throughout the porewater (Fig. 2). A sensitivity analysis adding

98   additional dissolved Fe or DIC raised the saturation index only slightly; the most significant

99   increase in siderite saturation scenarios came from increasing pH from 6.8 (the assumed

100   porewater value) to 7.5 (Figure 2), consistent with observations from ferruginous porewaters,

101   where alkalinity increases alkalinity due to organic carbon remineralization (Vuillemin et al.,

102   2023).

103

104   **Figure 2** Bulk sediment and porewater geochemistry for the CL sediment core. **(a)** Porosity and

105   organic carbon content of the sediments. The high organic carbon content of the sediments

106   contributes to their high porosity. **(b)** Bulk sediment Fe and Mn content showing peaks at ~60

107   cm depth, which correspond to the presence of siderite (Figure 3). **(c)** Iron speciation analysis

108   demonstrating that much of the sediment Fe is contained in the $Fe(II)_{unsulf}$ pool. **(d)** Porewater

109   dissolved inorganic carbon (DIC) concentration and isotope composition, showing a positive δ

110   ^{13}C signature consistent with the mass balance of depleted carbon lost to methanI**(e)** Siderite

111   saturation index (SI), which assumes the Fe concentration (1.689 mmol/L) and pH (6.8) of

112   deepest ferruginous water and measured porewater DIC values. Sensitivity scenarios were based

113   on doubling DIC and Fe concentrations, and increasing pH to 7.5.

114

115   Siderite was detected by XRD, with primary and secondary peaks observed at 31.62° and 52°

116   2θ (Fig. 3). A semiquantitative ratio of siderite to quartz (I_{sid}/I_{qtz}) suggests siderite is

117   concentrated mid-core (~60 cm), despite being supersaturated throughout the porewaters. SEM

118   images from this interval detected < 5 μm globular clumps with both dumbbell and spherical

119   egg-shaped siderite morphologies that are consistent with growth in an organic matrix (Dupraz et

120   al., 2009); a few crystals also exhibited rhomb-like shapes. All observed crystal forms were

121   consistent with siderite crystals grown in lab experiments (*e.g.,* Jiang and Tosca, 2019; Lin *et al.,*

122   2019) or observed in lacustrine settings (Wittkop et al. 2014). Pre-edge peak fitting of sediment

123   Fe XANES indicated predominantly Fe(II) (see SI). Iron EXAFS of sediments were best fit by

124   combinations of Bio Fe and siderite, with siderite having the greatest fit contribution (20.8 %) at

125   64 cm. Manganese XANES spectra were consistent with rhodochrosite ($MnCO_3$, which forms

126   solid solutions with siderite) in samples from 64 and 110 cm.

127

128   **Figure 3** Sediment Fe phases. **(a)** Example XRD scans showing the emergence of siderite in

129   mid-core depths (57.5 and 63.5 cm scans; Q = quartz peaks, S = siderite peaks). **(b)** Relative

130   XRD intensity of the siderite peak normalized to the quartz peak (I_{sid}/I_{qtz}), showing an increase in

131   siderite abundance mid-core. **(c)** Sediment Fe EXAFS spectra fit with linear contribution,

132   showing values for Bio Fe, greigite, and siderite, with the greatest contribution (20%) of siderite

133   to fits in the 64 cm samples (Table S-5a). **(d)** Sediment Mn XANES dominated by reduced

134   Mn(II), and the emergence of a distinctive double-peak of rhodochrosite in the 64 and 110 cm

135   samples. **(e-f)** Example SEM images of twinned sphere and dumbbell crystal morphologies from

136   the siderite-enriched interval, consistent with experimental precipitates of the mineral.

137

138 **Primary Iron Phases in Canyon Lake**

139 Despite the highly reducing nature of the CL water column and sediments, some Fe_{ox1} persists in

140 the sediment core. XANES spectra are consistent with the presence of mixed Fe(II)-Fe(III)

141 phases (see SI), perhaps green rust, which has been found in other ferruginous settings (Zegeye

142 *et al.,* 2012). While authigenic magnetite has also been shown to be an early precipitate in

143 ferruginous settings (Bauer *et al.,* 2020), the concentrations in our extractions were very low

144 (Fig. 2), and magnetite was not conclusively detected by EXAFS or XRD. Our EXAFS results

145 suggest greigite is present in the sediments, but Fe extractions imply that this mixed-valence

146 sulfide is a minor component of the Fe_{HR} pool (*i.e.,* low concentrations of Fe sulfides),

147 suggesting that the EXAFS analysis is highly sensitive to the presence of sulfides, or is perhaps

148 interfered with by an unknown phase. Sulfide abundance is limited by the small sulfate reservoir

149 in the water column available for reduction (Lambrecht et al., 2018), though a contribution from

150 an organic sulfur reservoir cannot be ruled out (e.g. Phillips et al., 2023).

151

152 The persistence of reduced Mn phases throughout the CL water column and sediments (Figs. 1

153 and 2) underscores the limited ability of this system to oxidize the large reservoir of Fe and Mn

154 from the ferruginous portion of the water column. The dominance of reduced Mn phases in

155 sediment trap materials perhaps points to an external source of reduced solutes—in this case,

156 groundwater input to the lake (Lambrecht *et al.*, 2018). Thus Fe(III) delivery to CL sediments is

157 limited, likely in the form of a poorly ordered Fe-(oxyhydr)oxide (Bio Fe), potentially

158 supplemented by small quantities of greigite and/or green rust; a small component of Fe(III) may

159 be added through detrital phases.

160

161 **Controls on Siderite Occurrence**

162 Although equilibrium modelling indicates siderite supersaturation throughout CL porewaters,

163 carbonate minerals were only confirmed in one relatively restricted horizon, suggesting an

164 inhibiting factor in the remaining intervals. The relatively slow kinetics of siderite precipitation,

165 especially in the cold (~5 °C) bottom waters of CL, is a likely constraint; hence, a metastable

166 precursor to siderite such as green rust may precipitate first. Carbonate green rust is closely

167 associated with diagenetic siderite precipitation (Vuillemin *et al.,* 2019), and has been previously

168 identified in the sediment traps from ferruginous Lake Matano (Zegeye *et al.,* 2012). Green rust

169 ages to siderite in laboratory experiments (Halevy *et al.,* 2017), but the mechanisms which

170 govern this transformation are not well understood (*e.g.,* Wiesli *et al.,* 2004), though pH is an

171 important control on its behavior (e.g. Guilbaud *et al.*, 2013). Although green rust potentially

172 plays a role in the CL system, we were not able to conclusively identify it in this study.

173

174 The organic-carbon rich CL sediments also create an environment that inhibits carbonate

175 precipitation. Over longer timescales, porewater alkalinity and pH are known to increase due to

176 continued OM fermentation (Vuillemin *et al.,* 2023), but organic substrates may both inhibit and

177 promote carbonate precipitation, dependent on the composition of functional groups, and the pH

178 of the environment (Dupraz *et al.,* 2009). In CL sediments, intense fermentation (Lambrecht *et*

179 *al.,* 2020) likely contributes to the inhibition of siderite precipitation by adding CO_2 to the pore

180 fluids, buffering against significant increases in pH.

181

182 The appearance of crystalline siderite (XRD-detectable) ~60 cm below the ferruginous sediment-

183 water interface suggests a precipitation barrier was overcome in this horizon, likely by an

184   environmental change. While porewater diffusion smoothes the concentration profiles of solutes,

185   diagenetic siderite precipitation may occur episodically due to environmental changes, such as

186   lake level fluctuations (*e.g.,* Vuillemin *et al.,* 2023). However, CL has been stably stratified at

187   least since the late 1930s (Lambrecht *et al.,* 2018), implying that climate-driven changes in lake

188   mixing (*e.g.,* drought) were an unlikely influence in the interval where siderite occurs (see SI).

189   Wildfires are a more likely influence, as both historical accounts and tree-ring records indicate

190   that significant fires occurred in the forests surrounding CL as recently as the early 1900s

191   (Muzika *et al.,* 2015). Calcium carbonate is a known product of wood combustion, and wildfire

192   mineral ash is known to increase environmental pH in a variety of contexts (*e.g.,* Brito *et al.,*

193   2021).

194

195   Mineral ash deposition would stimulate an increase in porewater pH and deliver $CaCO_3$ to

196   sediments. These changes would catalyse siderite precipitation by enhancing sorbtion of Fe and

197   Mn ions to ash particles (Brito *et al.*, 2021), increasing the activity of CO_3^{2-} (Fig. 4), and

198   providing nucleation sites for crystal growth, overcoming kinetic barriers to siderite precipitation

199   (Jiang and Tosca, 2019; Lin *et al.*, 2019). The increase in abundance of bulk Fe and Mn in the

200   siderite layer (Figure 2) is consistent with a sorbtive process, and an ash layer may have resulted

201   in reduced sediment porosity in the same interval, impeding porewater flow, leading to a

202   localized increase in solute concentrations, further enhancing mineral precipitation potential.

203   These observations suggest that the siderite layer in Canyon Lake sediments derives from a

204   combination of depositional (ashfall, sorbtion) and diagenetic (post-depositional crystal growth)

205   processes.

206

207   We cannot eliminate the possibility that another process such as an overturn of lake stratification

208   drove enhanced Fe(III) delivery to CL sediments in the past, but it seems unlikely. Lake overturn

209   would presumably be accompanied by oxidation of the CL's large isotopically light methane

210   reservoir, which is inconsistent with our carbon isotope data. The association between mineral

211   ash fall and sidertite precipitation we suggest is testable with high-resolution sediment

212   chronology, advanced microscopy (e.g. TEM), and/or charcoal analysis.

213

214   The pronounced influence of pH on siderite precipitation is linked to the dependence of siderite

215   saturation on the concentration of the CO_3^{2-} ion (Fig. 4). Carbonate equilibrium dictates that

216     $[CO_3^{2-}]$ scales linearly with total DIC but nonlinearly with $[H^+]$, due to the presence of a

217   quadratic term (SI). Hence, changing the pH by 1 unit has a stronger effect than a more

218   substantial change in DIC. In CL porewaters where organic carbon remineralization buffers H^+

219   fluctuations by increasing alkalinity (and consumption of H^+ by acetogens and methanogens), an

220   external agent (i.e. mineral ash) is required to drive more substantial pH changes.

221

222   **Figure 4** Relative influence of changes in porewater Fe concentration, pH and DIC on the

223   saturation index of siderite. Inputs are based on water chemistry at 20 m, which is assumed to

224   represent a minimum threshold for porewater concentrations. In general, iron concentrations

225   above ~100 μM seem to be required for siderite precipitation, unless the pH is high.

226

227   The detection of rhodochrosite by XANES in the same horizon where XRD indicates siderite

228   illustrates the heterogeneous nature of carbonate precipitation in CL. Lacustrine siderites are

229   commonly Mn-substituted (Swanner *et al.,* 2020), possibly linked to the more readily reducible

230   nature of Mn-oxides relative to Fe-(oxyhydr)oxides (Vuillemin *et al.,* 2019). However, the lack

231   of an Mn-oxide flux in CL suggests a fundamental control on precipitation explains this

232   occurrence of Mn-siderite, with competition from nucleation inhibitors (*e.g.,* Mg(II); Vuillemin

233   *et al.,* 2019) or the differential solubilities of Ca-Mn-Fe carbonates (*e.g.,* Wittkop *et al.,* 2020)

234   offering potential explanations. Thus, the occurrence of Mn-rich siderite in the geologic record

235   (*e.g.,* Siahi *et al,* 2020; Swanner *et al.,* 2020) may be interpreted to reflect passive incorporation

236   of dissolved Mn into the crystal structure, rather than reduction of Mn-oxides.

237

238   **Biogeochemical Implications**

239   Although siderite occurs in sediments throughout the geologic record, direct precipitation from

240   Fe-enriched anoxic fluids is thought to be rare due to the slow kinetics of siderite precipitation

241   (Jiang and Tosca, 2019). Modern process studies in oxygenated surface environments tend to

242   encounter siderite only in early diagenetic settings (*e.g*., Lin *et al.,* 2020). Hence it is often

243   assumed that siderite precipitates following the deposition of an Fe-(oxyhydr)oxide precursor

244   such as ferrihydrite, which is subsequently reduced in the sediments through microbial

245   respiration, providing both dissolved Fe and the alkalinity needed to precipitate carbonate phases

246   (Heimann *et al.,* 2010). However, our observations are not consistent with this traditional model,

247   as the sediment Fe reservoir in CL is dominated by Fe(II) phases occurring below a persistently

248   ferruginous water column.

249

250   While Fe-(oxyhydr)oxides are often invoked as precursors for Precambrian iron formation (IF)

251   deposition (*e.g.,* Konhauser *et al.,* 2017), recent work has focused on the role of Fe-silicates in IF

252   genesis (*e.g.,* Hinz *et al.,* 2021). In CL, direct precipitation of siderite below a ferruginous water

253   column represents a significant Fe burial pathway that does not require precursor Fe-

254   (oxyhydr)oxides or silicates. Hence, our work demonstrates that the presence of siderite in

255   sediments should be carefully considered when interpreting past redox conditions, as direct

256   precipitation pathways imply much lower oxygen levels at the sediment-water interface than

257   diagenetic pathways involving Fe-(oxyhydr)oxide reduction.

258

259   Multiple studies highlight the importance of pH in governing both Fe-carbonate and Fe-silicate

260   systems (Halevy *et al.,* 2017; Jiang and Tosca, 2019; Hinz *et al.,* 2021), as well as the evolution

261   of stable phases from green rust precursors (Zegeye *et al.,* 2012). Could subtle variations in

262   seawater silica concentration and pH have generated the silicate-carbonate banding observed in

263   many Precambrian IFs (*e.g.,* James *et al.*, 1968; Beukes *et al.,* 1990)? A growing body of

264   evidence supports this possibility, but additional experiments are needed to evaluate the role of

265   pH changes and the presence of nucleation substrates in the direct precipitation of siderite (and

266   associated Mn-carbonate).

267

268   In ancient seas, the role of wildfire ash in CL may have been played by processes that introduce

269   calcium carbonate to more acidic ferruginous waters, including transgression over previously

270   deposited carbonates, turbidites, or crystals settling from whiting events (*e.g.,* Morse *et al.,*

271   2003). The novel link between wildfire ash and enhanced siderite precipitation identified here

272   may also imply a new pathway for enhancing carbon sequestration in methane-rich, ferruginous

273   environments that appear to be widespread in boreal shield settings and postglacial lakes (Schiff

274   *et al.,* 2016).

275

276 **ACKNOWLEDGMENTS**

286

287 **REFERENCES CITED**

288

289 Bauer, K.W., Byrne, J.M., Kenward, P., Simister, R.L., Michiels, C.C., Friese, A., Vuillemin, A.,

290 Henny, C., Nomosatryo, S., Kallmeyer, J., Kappler, A., Smit, M.A., Francois, R., and

291 Crowe, S.A. (2020) Magnetite biomineralization in ferruginous waters and early Earth

292 evolution. *Earth and Planetary Science Letters* 549, 116495,

293 https://doi.org/10.1016/j.epsl.2020.116495

294

295 Beukes, N.J., Klein, C., Kaufman, A.J., and Hayes, J.M. (1990) Carbonate petrography, kerogen

296 distribution, and carbon and oxygen isotope variations in an Early Proterozoic transition

297 from limestone to iron-formation deposition, Transvaal Supergroup, South Africa.

298 *Economic Geology* 85, p. 663-690

299

300   Brito, D.Q., Santos, L. H. G., Passos, C.J.S., and Oliveira-Filho, E.C. (2021) Short-Term Effects

301   of Wildfire Ash on Water Quality Parameters: A Laboratory Approach. *Bulletin of*

302   *Environmental Contamination and Toxicology* 107, 500-505, https://doi.org/10.1007/s00128-

303   021-03220-9.

304

305   Dupraz, C., Reid, R. P., Braissant, O., Decho, A. W., Norman, R. S., & Visscher, P. T. (2009).

306   Processes of carbonate precipitation in modern microbial mats. *Earth-Science Reviews*, 96(3),

307   141–162. https://doi.org/10.1016/j.earscirev.2008.10.005

308

309   Guilbaud, R., White, M.L., and Poulton, S.W. (2013). Surface charge and growth of sulphate and

310   carbonate green rust in aqueous media. *Geochimica et Cosmochimica Acta* 108, 141-153.

311

312   Halevy, I., Alesker, M., Schuster, E.M., Popovitz-Biro, R., and Feldman, Y. (2017) A key role

313   for green rust in the Precambrian oceans and the genesis of iron formations. *Nature Geoscience*,

314   https://doi.org/10.1038/NGEO2978.

315

316   Hansel, C. M., Benner, S.G., and Fendorf, S, (2005) Competing Fe(II)-Induced Mineralization

317   Pathways of Ferrihydrite. *Environmental Science & Technology*, 39: 7147–7153.

318   https://doi.org/10.1021/es050666z

319

320   Heimann, A., Johnson, C.M., Beard, B.L., Valley, J.W., Roden, E.E., Spicuzza, M.J., and

321   Beukes, N.J. (2010) Fe, C, and O isotope compositions of banded iron formation carbonates

322   demonstrate a major role for dissimilatory iron reduction in ~2.5 Ga marine environments. *Earth*

323   *and Planetary Science Letters* 294, 8-18.

324

325   Hinz, I., Nims, C., Theuer, S., Templeton, A.S., and Johnson, J.E. (2021) Ferric iron triggers

326   greenalite formation in simulated Archean seawater. *Geology* 49, 905- 910,

327   https://doi.org/10.1130/G48495.1.

328

329   James, H.J., Dutton, C.E., Pettijohn, F.J., and Wier, K.L. (1968) Geology and Ore Deposits of

330   the Iron River-Crystal Falls District, Iron Country, Michigan. Geological Survey Professional

331   Paper 570, https://doi.org/10.3133/pp570.

332

333   Jiang, C.Z., and Tosca, N.J. (2019) Fe (II)-carbonate precipitation kinetics and the chemistry of

334   anoxic ferruginous seawater. *Earth and Planetary Science Letters*, 231-242.

335

336   Konhauser, K. O., Planavsky, N. J., Hardisty, D.S., Robbins, L.J., Warchola, T.J., Haugaard, R.,

337   Lalonde, S.V., Partin, C.A., Ooonk, P.B.H., Tsikos, H., Lyons, T.W., Bekker, A., Johnson, C.M.

338   (2017) Iron Formations: A global record of Neoarchean to Paleoproterozoic environmental

339   history. *Earth-Science Reviews*, 140-177.

340

341   Lambrecht, N., Katsev, S., Wittkop, C., Hall, S. J., Sheilk, C.S., Picarad, A., Fakhraee, M., and

342   Swanner, E. D. (2020) Biogeochemical and physical controls on methane fluxes from

343   two ferruginous meromictic lakes. *Geobiology*, https://doi.org/10.1111/gbi.12365.

344

345   Lambrecht, N., Wittkop, C., Katsev, S., Fakhraee, M., and Swanner, E. D. (2018) Geochemical

346   Characterization of Two Ferruginous Meromictic Lakes in the Upper Midwest, USA. *Journal of*

347   *Geophysical Research: Biogeosciences*, 123, 3403-3422,

348   http://dx.doi.org/10.1029/2018JG004587.

349

350   Lin, C. Y., Turchyn, A.V., Krylov, A., and Antler, G. (2019) The microbially driven formation

351   of siderite in salt marsh sediments. *Geobiology* 18, 207-224, https://doi.org/10.1111/gbi.12371.

352

353   Morse, J.W., Gledhill, D.K., and Millero, F.J. (2003) $CaCO_3$ precipitation kinetics in waters

354   from the great Bahama bank: Implications for the relationship between bank hydrochemistry and

355   whitings. *Geochimica et Cosmochimica Acta* 67, 2819-2826, https://doi.org/10.1016/S0016-

356   7037(03)00103-0.

357

358   Muzika, R.M., Guyette, R.P., Stambaugh, M.C., and Marschall, J.M. (2015) Fire, Drought, and

359   Humans in a Heterogeneous Lake Superior Landscape. *Journal of Sustainable Forestry* 34, 49-

360   70, https://doi.org/1080/10549811.2014.973991.

361

362   Ohmoto, H., Watanabe, Y., and Kumazawa, K. (2004) Evidence from massive siderite beds for a

363   CO_2-rich atmosphere before ~ 1.8 billion years ago. *Nature* 429, 395-399.

364

365   Phillips, A.A., Ulloa, I., Hyde, E., Agnich, J., Sharpnack, L., O'Malley, K.G., Webb, S.M.,

366   Schreiner, K.M., Sheik, C.S., Katsev, S., and Raven, M.R. (2023) Organic sulfur from source to

367   sink in low-sulfate Lake Superior. Limnology and Oceanography 68, 2716-2732,

368   https://doi.org/10.1002/lno.12454.

369

370   Riding, R., Liang, L., and Fralick, P. (2022) Oxygen-induced chemocline precipitation between

371   Archean Fe-rich and Fe-poor carbonate seas. *Precambrian Research* 383, 106902,

372   https://doi.org/10.1016/j.precamres.2022.106902

373

374   Schiff, S.L., Tsuji, J.M., Wu, L., Venkiteswaran, J.J., Molot, L.A., Elgood, R.J., Paterson, M.J.,

375   and Neufeld, J.D. (2016) Millions of boreal shield lakes can be used to probe Archean ocean

376   biogeochemistry. *Scientific Reports* 7, 46708 (2017), https://doi.org/10.1038/srep46708.

377

378   Siahi, M., H. Tsikos, S. Rafuza, P. B. H. Oonk, X. R. Mhlanga, D. van Niekerk, P. R. D. Mason,

379   and C. Harris (2020) Insights into the processes and controls on the absolute abundance and

380   distribution of manganese in Precambrian iron formations. *Precambrian Research* 350: 105878.

381   https://doi.org/10.1016/j.precamres.2020.105878.

382

383   Swanner, E.D., Lambrecht, N., Wittkop, C., Harding, C., Katsev, S., Torgeson, J., and Poulton,

384   S.W. (2020) The biogeochemistry of ferruginous lakes and past ferruginous oceans:

385   *Earth-Science Reviews* 211, 1-43, https://doi.org/10.1016/j.earscirev.2020.103430.

386

387   Toner, B.M., Santelli, C.M., Marcus, M.A., Wirth, R., Chan, C.S., McCollom, T., Bach, W., and

388   Edwards, K.J. (2009) Biogenic iron oxyhydroxide formation at mid-ocean ridge hydrothermal

389   vents: Juan de Fuca Ridge. *Geochimica et Cosmochimica Acta* 73, 388–403,

390   https://doi.org/10.1016/j.gca.2008.09.035.

391

392   Vuillemin, A., Wirth, R., Kemnitz, H., Schleicher, A.M., Friese, A., Bauer, K.W., Simister, R.,

393   Nomosatryo, A., Ordonez, L., Ariztegui, D., Henny, C., Crowe, S. A., Benning, L. G.,

394   Kallmeyer, J., Russell, J. M., Bijaksana, S., Vogel, H., and the Towuti Drilling Project Science

395   Team (2019) Formation of diagenetic siderite in modern ferruginous sediments. *Geology*,

396   https://doi.org/10.1130/G46100.1.

397

398   Vuillemin, A., Mayr, C., Schuessler, J. A., Friese, A., Bauer, K. W., Lücke, A., Heuer, V.B.,

399   Glombitza, C., Henny, C., von Blanckenburg, F., Russell., J.M., Bijaksana, S., Vogel, H., Crowe,

400   S.A., and Kallmeyer, J. (2023). A one-million-year isotope record from siderites formed in

401   modern ferruginous sediments. *Geological Society of America Bulletin*, 135(1–2), 504–522.

402   https://doi.org/10.1130/B36211.1.

403

404   Wiesli, R.A., Beard, B.L., Johnson, C.M. (2004) Experimental determination of Fe isotope

405   fractionation between aqueous Fe(II), siderite and "green rust" in abiotic systems. *Chemical*

406   *Geology* 211, 343–362.

407

408   Wittkop, C., Swanner, E., Grengs, A., Lambrecht, N., Fakrhaee, M., Myrbo, A., Bray, A.,

409   Poulton, S., and Katsev, S. (2020) Evaluating a primary carbonate pathway for manganese

410   enrichments in reducing environments. *Earth and Planetary Science Letters* 538, 116201,

411   https://doi.org/10.1016/j.epsl.2020.116201.

412

413 Zegeye, A., Bonneville, S., Benning, L.G., Sturm, A., Fowle, D.A., Jones, C., Canfield, D.E.,

414 Ruby, C., MacLean, L.C., Nomosatryo, S., Crowe, S.A., Poulton, S.W. (2012) Green rust

415 formation controls nutrient availability in a ferruginous water column. *Geology* 40, 599–602,

416 https://doi.org/10.1130/g32959.1.
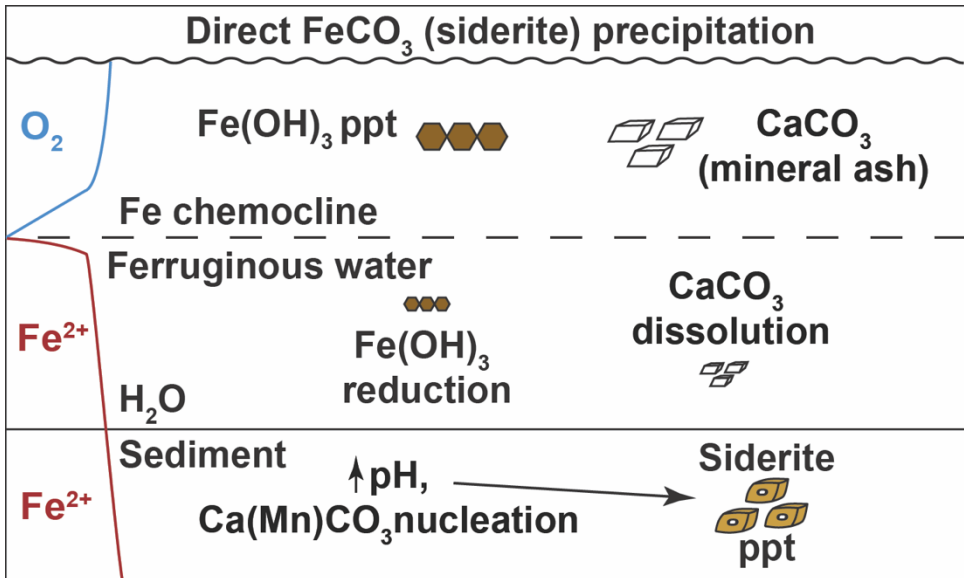
417

Graphic abstract

Direct FeCO$_3$ (siderite) precipitation

O$_2$

Fe(OH)$_3$ ppt

CaCO$_3$
(mineral ash)

Fe chemocline

Ferruginous water

Fe^{2+}

Fe(OH)$_3$
reduction

CaCO$_3$
dissolution

H$_2$O

Sediment

Fe^{2+}

↑pH,
Ca(Mn)CO$_3$ nucleation

Siderite

ppt

Figure 1

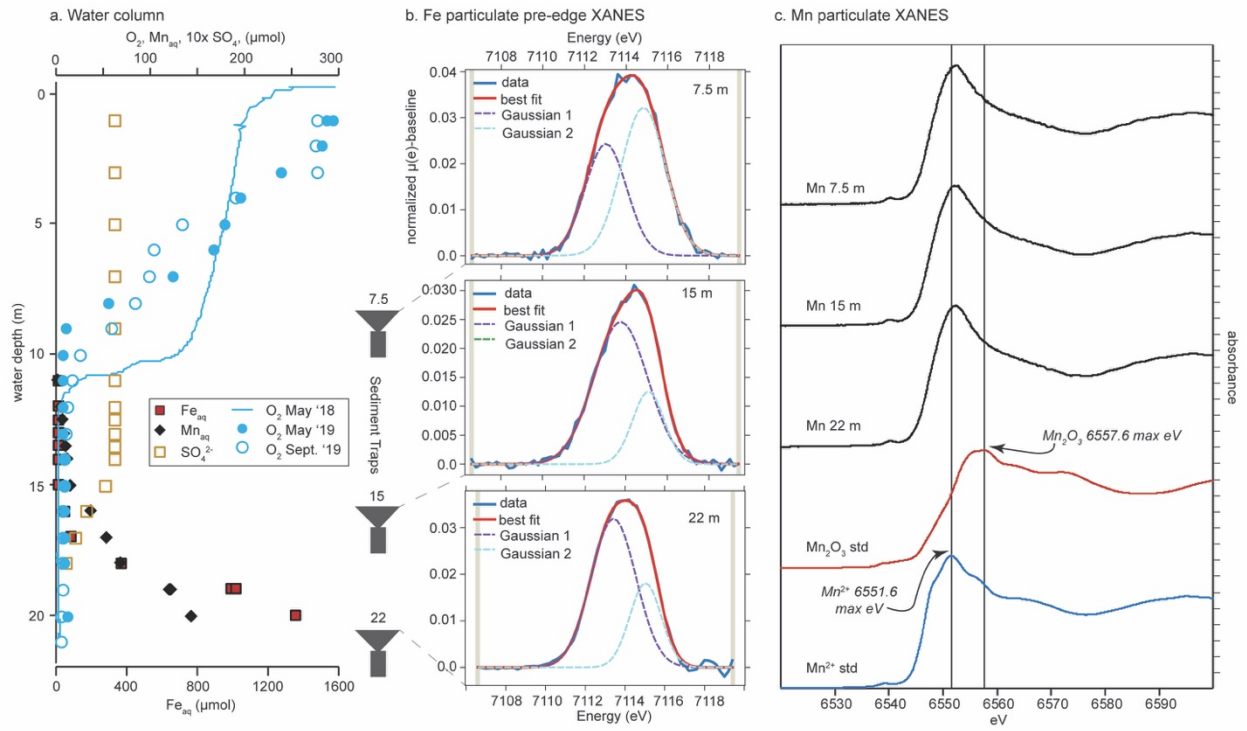a. Water column

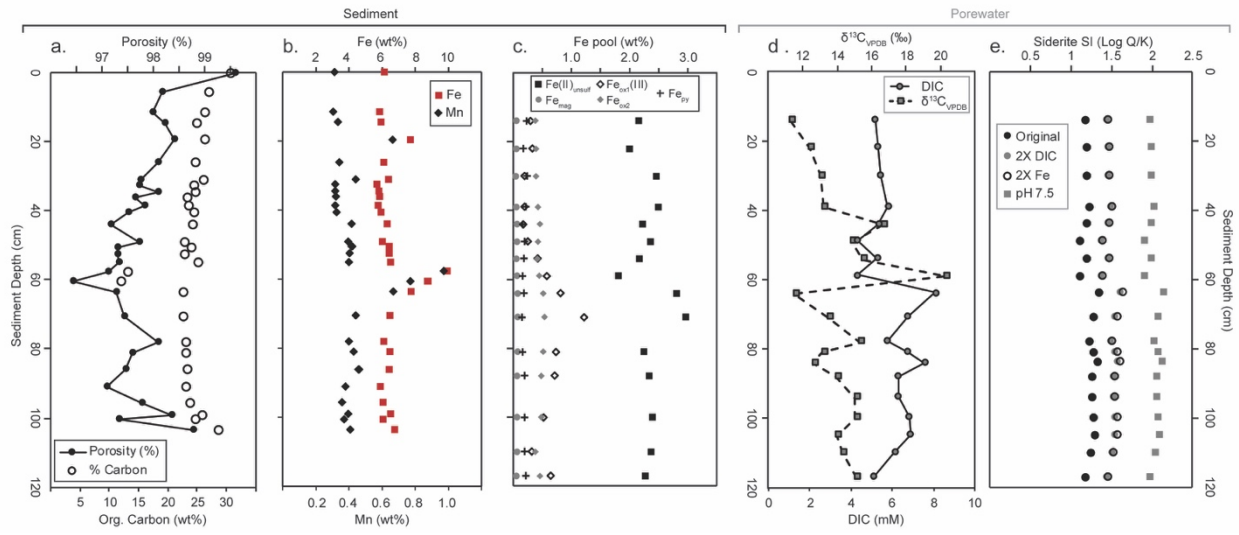b. Fe particulate pre-edge XANES

c. Mn particulate XANES
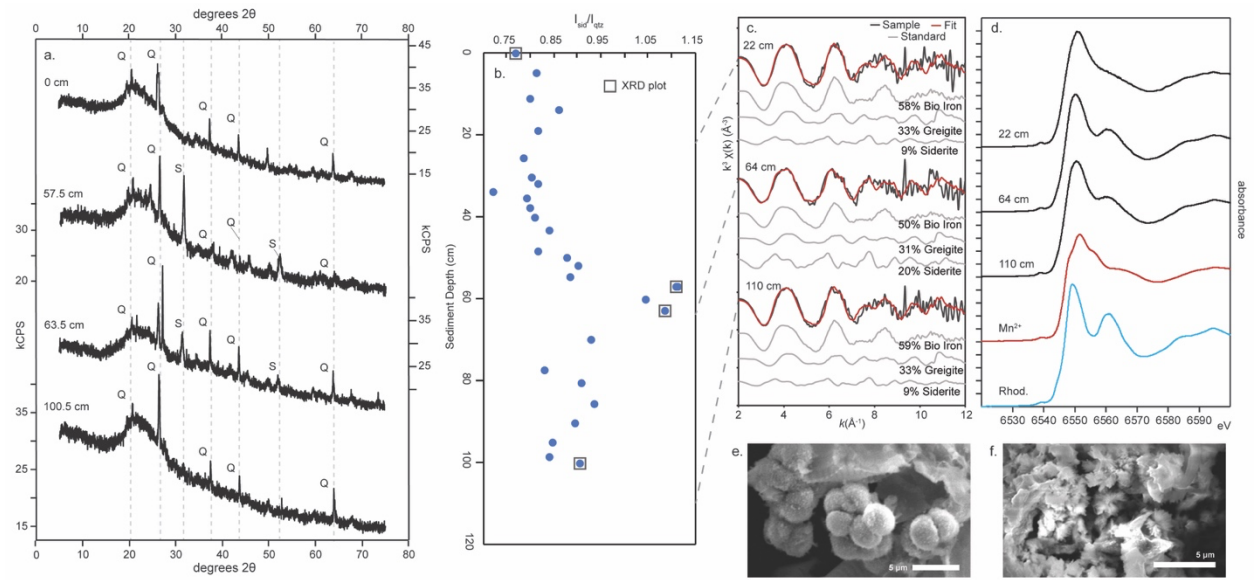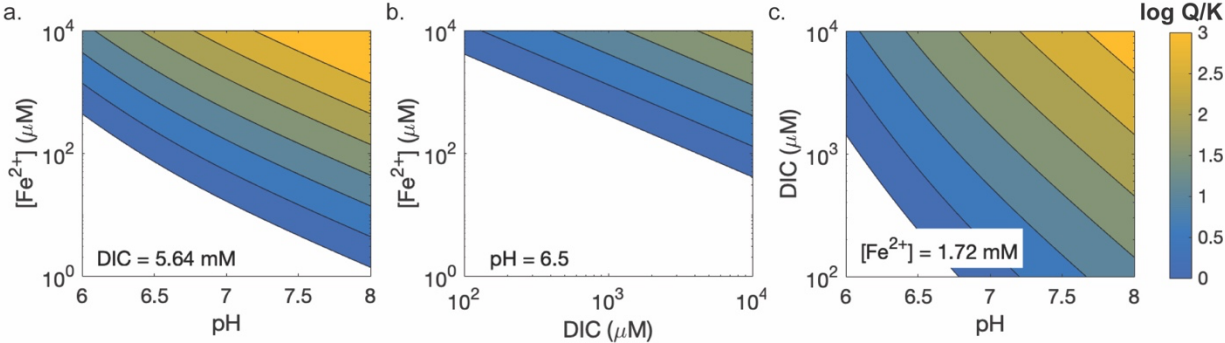
Figure 2

Figure 3

Figure 4

Direct precipitation of siderite in ferruginous environments

A. Grengs, G. Ledesma, Y. Xiong, S. Katsev, S.W. Poulton, E.D. Swanner, and C. Wittkop

Supplementary Information

The Supplementary Information includes:

- ➢ Study Site
- ➢ Methods
- ➢ Results
- ➢ Discussion
- ➢ X-ray Absorption Spectra Supplementary Results and Discussion
- ➢ Tables S-1 to S-5
- ➢ Figures S-1 to S-7
- ➢ Raw Data including Sample Depths, XRF, XRD, Elementar CS
- ➢ Supplementary Information References

Study Site

Canyon Lake is located at N46°49'58.069", W87°55'14.858", within the temperate upper peninsula of Michigan, USA. The lake is located on private property owned by the Huron Mountain Club, in an area consisting of coniferous forest on a substrate of Archean gneiss and relatively thin Pleistocene glacial deposits. Canyon Lake and its immediate catchment are undeveloped and managed as a wilderness area. The lake has a surface area of 1 hectare and maximum depth of 23 m (Lambrecht *et al.,* 2018). There is no surface inflow to the lake; groundwater supplies solutes, and a small stream flows out. The lake experiences limited wind mixing due to shelter from gneiss outcrops that are up to 20 m in height.

Water Column Properties

The iron chemocline is ~17 m deep. Above the chemocline, the water column is typically split into an oxic surface layer (~0-8 m), and an anoxic middle layer (~8-17 m), which mix seasonally. Below the chemocline, dissolved iron concentrations increase rapidly to a relatively constant concentration of ~1600 μM in its deepest waters (Lambrecht *et al.,* 2020; Swanner *et al.*, 2021). There is no evidence of mixing of the water mass below the chemocline since at least the late 1930's (Lambrecht *et al.,* 2018).

Methods

Water Column Geochemistry

Canyon Lake water column geochemistry methods and data from 2015-2019 were previously reported in Swanner *et al.* (2021). Standard techniques were utilized, including *in situ* sensor monitoring of dissolved oxygen, and inline filtration (to 0.45 μm) for cation (acid preserved) and anion samples.

Sediment Sample Collection and Preparation

Sediment Traps. Canyon sediment traps were deployed May through September 2019 (114 days). Canyon traps utilized funnels with a 346.36 cm^2 diameter due to the low sedimentation rate in the system. Three traps were deployed in Canyon Lake at the 7.5, 15 and 20 m water depths to capture phases from the oxic, chemocline and anoxic layers, respectively. Due to the wilderness nature of the environment, biological poisons were not used in the traps. Recovered trap solids were immediately subsampled under a nitrogen (N_2) atmosphere, and samples for XANES and EXAFS analysis were stored anoxically in an N_2-filled airtight container.

Sediment Freeze Core. In February 2018, a 103.5 cm-length sediment core was obtained from Canyon Lake's deepest point using an aluminium frozen wedge freeze corer chilled with a mixture of dry ice and ethanol (e.g., Wright, 1980). The core was lowered into the sediments and held in position using drive rods for ten minutes. The recovered core was transported on dry ice and subsequently stored at -80 °C. The recovered freeze core was subsequently sectioned and subsampled at the LacCore Facility at the University of Minnesota, and at Iowa State University. The core was maintained at -80 °C with dry ice during handling but was thawed once it was brought into a 100% N_2 glovebox (Ledesma et al., 2023). Some variations in sample intervals and features observed by core depth occurred due to variations in the sediment, and breakages that occurred in the frozen blocks during recovery and transport.

Porewaters were extracted from sediments inside an anoxic glovebox using Rhizon samplers (Islam, 2022), and δ13C and dissolved inorganic carbon (DIC) were determined by measuring gas evolved from 1 mL of sample water injected into Exetainers pre-loaded with concentrated phosphoric acid, as previously detailed (Lambrecht *et al.,* 2020). Porosity (n) was calculated from freeze core samples by recording the subsample's initial mass, then melting the frozen sediment chunks in a 50 mL centrifuge tube to obtain a sample volume. Samples were then freeze dried and a dry sample weight was reached. From this data we were able to obtain the bulk density (ρ_b) and assumed that the particle density (ρ_d) was 2.6 g/mL. The equation used was n = (1 - (ρ_b/ρ_d)) * 100 % (Eq. S-1).

Constraints on Sediment Age

Our study did not collect sediment age data, but radiocarbon dates on a long sediment core collected in 1970 from Canyon Lake are available in the Neotoma Database (https://data.neotomadb.org/15682, https://doi.org/10.21233/zpe5-s053). A simple linear age model based on the calibrated ages (IntCal13) of the two uppermost dates (150 and 295 cm below lake floor) yields an average sedimentation rate of 0.1 cm/yr. Based on these constraints, the siderite zone at approximately 60 cm depth would have been deposited within the past 600 years. While this places a maximum age constraint on our sediments, it is likely a significant underestimate of the actual sedimentation rate, which would be higher in unconsolidated surface sediments.

Geochemical Analyses

XRF. Freeze dried samples were prepared for XRF by first homogenizing them with a mortar and pestle into finer particles. Then samples were individually weighed with masses ranging from 0.4745 to 1.4448 g, depending on sediment textures and compositions. These loose powder samples were placed into a polyethylene cup (SPEX 3527 40 mm X-Cell) and covered with 3.0 μm Etnom film. Samples were analysed on a Rigaku Supermini 200 XRF Spectrometer

under a helium atmosphere with Pd-anode X-rays at 50 kV and 4.0 mA. Samples were rotated, with a total scan time of ~45 minutes per sample.

XRD. Following XRF, samples were prepared for powder XRD. The samples were loaded into aluminium holders and loosely packed with a smoother. Samples were analysed on a Rigaku Ultima IV with a Cu-Kα radiation source, and an X-ray energy of 40 Ma and 44 kV. Samples were scanned from 5 to 75 ° 2θ with 0.02 ° intervals.

We examined the ratio of siderite peak area between 31.1 ° to 32.1 ° 2θ in comparison to quartz peak area between 26.1 ° to 26.9 ° 2θ to provide a semiquantitative siderite to quartz ratio (I_{sid}/I_{qtz}). Quartz was chosen as a basis for this ratio on the assumption of a relatively constant amount of quartz in the samples. Thus, when the I_{sid}/I_{qtz} is greater than one, it is interpreted to contain siderite.

Elementar CS. Freeze-dried and homogenized samples were analysed for total carbon and sulphur content using an Elementar CS cube elemental analyser. To remove carbonate phases, the samples were weighed into silver capsules, wetted with a small amount of MQ water and put in a fumigation chamber with a beaker containing 12 M HCl for 6 hours. After removal from the fumigation chamber, samples were dried on a hotplate for 48 hours and wrapped in a tin capsule before being analysed (Harris *et al.,* 2001).

Iron Phase Partitioning. The phase partitioning of Fe was determined via the sequential extraction techniques of Canfield *et al.* (1986) and Poulton and Canfield (2005), with the latter modified for application to modern sediments (Zegeye *et al.,* 2012; Poulton, 2021). Iron present as acid volatile sulfide (Fe_{AVS}) was extracted by a concentrated HCl extraction and was below detection (<0.001), followed by a chromous chloride extraction to dissolve pyrite (Fe_{py}), with the sulfide liberated from each extraction being fixed as Ag_2S (Canfield *et al.,* 1986). Iron concentrations were then determined gravimetrically. Operationally-defined non-sulfidic Fe phases were initially extracted with 0.5 N HCl for 1 hour. This extraction dissolves phases such as Fe_{AVS}, surface-reduced Fe(II), poorly crystalline Fe carbonates, green rust and poorly crystalline hydrous ferric oxides such as ferrihydrite (Poulton, 2021). The reduced Fe phases ($Fe(II)_{unsulf}$) in this extract were immediately determined by spectrophotometer using the ferrozine assay (Stookey, 1970), and Fe(III) (*i.e.* ferrihydrite; Fe_{ox1}) was determined via atomic adsorption spectroscopy (AAS) after subtraction of the Fe(II) phases (Zegeye *et al.,* 2012; Poulton, 2021). A sodium dithionite extraction was then used to dissolve crystalline Fe (oxyhydr)oxides (*e.g.,* goethite, hematite; Fe_{ox2}), which was followed by a sodium acetate extraction to dissolve magnetite (Fe_{mag}), with Fe in both extracts determined by AAS (Poulton and Canfield, 2005). Replicate extractions gave a relative standard deviation of < 5% for all phases.

Iron phase partitioning data are reported in Table S-1, and the highly reactive Fe fraction (Fe_{HR}) was determine as the sum of $Fe(II)_{unsulf} + Fe_{ox1} + Fe_{ox2} + Fe_{mag} + Fe_{py}$ (Xiong *et al.,* 2019). The ratios Fe_{HR}/Fe_T and Fe_{py}/Fe_{HR} were calculated and compared to calibrated thresholds for determining different water column redox states (Poulton and Canfield, 2011; Poulton, 2021). As expected, all data plot in the anoxic ferruginous field (Fig. S-1).

Microscopy. Scanning Electron Microscopy (SEM) and Energy Dispersive Analysis (EDS) were used to identify and characterize Fe- and Mn-bearing particulate phases. For this research, the EDS was used to identify particles containing Fe, Mn, S, P, Si, O, C, Ca and Mg. Samples for SEM-EDS analysis were selected from cores and traps. Homogenized samples were sprinkled onto a 10 mm aluminium mount with black carbon tape. The filtered samples were directly placed onto the carbon tape. Initial EDS analysis was performed on uncoated samples, with follow-up imaging work on carbon-coated samples. All samples were analysed on MNSU's JEOLJSM-6510LV/LGS SEM. The conditions were set to an accelerating voltage of 15.0 kV, working distance of 15 mm, and spot size of 60.

Mineral Saturation Analysis. Mineral saturation calculations were performed in Geochemists Workbench (GWB; Student Edition, Release 14) for purposes of evaluating the saturation state of siderite relative to a range of Fe and DIC concentrations and pH levels. The saturation state was modelled using the B-dot equation from the Debye-Huckel equation within GWB. A majority of water column data imported was from May 2018, including cation, anion, dissolved oxygen and temperature measurements; pH values were averaged from June 2015 and June 2017. Sediment freeze core DIC concentrations were used in GWB for modelling siderite saturation instead of the water column DIC concentrations (though water and sediment DIC concentrations were similar).

To assess siderite saturation states, the anoxic water depth of 20 m was selected to run different scenarios in GWB. Three scenarios were considered to evaluate single variable changes within the porewater, which included 1) multiplying Fe concentrations by 1.5, 2 and 2.5 times its original concentration, 2) doubling DIC concentrations, and 3) changing pH from 6 to 8 in half level increments.

The saturation index was calculated as log Q/K, where the solubility constant is $K = 10^{-10.45}$ and the activity product is $Q = [Fe^{2+}] [CO_3^{2-}]$. The influence of pH on carbonate mineral saturation is demonstrated from carbonate equilibria,

$$[CO_3^{2-}] = DIC \left(\frac{[H^+]}{K_2} + \frac{[H^+]^2}{K_1 K_2} + 1 \right)^{-1}$$

where $K_1 = 10^{-6.35}$, $K_2 = 10^{-10.33}$, and $[H^+] = 10^{(-pH)}$ (Eq. 1).

Under relevant environmental conditions, the concentration of H^+ is likely to vary across a wider range than the concentration of DIC and Fe. As a result, pH will be the strongest effect within a hypothetical system where Fe^{2+} and DIC concentrations are unlikely to vary significantly, though varying Fe^{2+} by orders of magnitude (*e.g.,* across different systems) can produce a similar effect on supersaturation.

The original inputs are presented in Tables S-2 and S-3. These tables contain values measured from 20 m water depth. To evaluate the saturation states of siderite, individual variables including Fe, HCO_3^- (DIC) and pH were changed as highlighted below. In the main text Figure 4, concentrations were used in place of activities to simplify the calculations, which may introduce an error at higher concentrations.

X-ray Absorption Spectra. Samples were finely powdered using a mortar and pestle inside a N₂ gas-filled glovebox. The powders were pressed into 7 mm pellets and loaded into custom sample holders using carbon tape to secure the pellets to the holder. These holders were transported to the beamline inside a heat-sealed mylar bag with oxygen-removing sachets. The Fe and Mn K-edge XANES analyses were performed at beamline 9-BM at the Advanced Photon Source of Argonne National Laboratory in fluorescence mode using a Vortex four element silicon drift detector with a Si(111) and Si(220) monochromator. Energy was calibrated with an Fe foil and the E0 set to 7112 eV, and a Mn foil with E0 set to 6539 eV. For sediments, three scans were collected per sample for Fe and six for Mn. For sediment traps, 10 scans were collected per sample for Fe and 15-20 for Mn. Channels were summed and deadtime corrected at the beamline. Scans were averaged and normalized in SixPack (Webb, 2005). Pre-edge peak fitting was done in XAS Viewer (Version Larch 0.9.58, https://xraypy.github.io/xraylarch/). Linear combination fitting (LCF) of Fe EXAFS was done in Athena (Version 0.9.26). Fits were performed from k 2-8 Å.

Results

Lake Properties

Consistent with previous observations (Lambrecht *et al.,* 2018; 2020), the Canyon Lake oxycline is positioned at ~12 m water depth, and an interval of low dissolved oxygen concentrations (typically between 1-10 µM) transitions to permanently ferruginous waters at a chemocline between 17-18 m. Strongly ferruginous waters (aqueous Fe concentrations up to ~1,600 µM) extend to the bottom, at ~23 m maximum depth. The pH of ferruginous waters near the sediment-water interface ranges from 6.2 to 7.1 (average = 6.5; Fig. S-2). The pH of the middle portion of the water column, where oxygen concentrations are low but dissolved Fe does not accumulate (6-14 m), are slightly lower (ranging from 5.6 to 6.9 at 12 m). The surface waters have consistently higher pH, ranging from 6.6 to 7.1.

Sediment Geochemistry and Mineralogy

The ferruginous sediments of Canyon Lake are exceptionally porous and rich in organic carbon (12.2 to 30.7 wt. %), with the two components linked: the high porosity is enabled both by water-rich sediments and easily displaced organic matter (and likely further displacement by subsequent freezing). Visual description indicates that the organic carbon fraction is largely allochthonous, consisting mainly of detritus from the landscape (pine needles, wood fragments), and the average C/N ratio of the sediment organic carbon is elevated (15.5), further suggesting a dominance of terrestrial sources (Meyers and Ishiwatari, 1993).

The average bulk concentration of Fe is 6.6 wt. %, but spikes to 9.9 wt. % Fe at ~60 cm depth. The concentration of Mn averages 0.44 wt. % but also spikes to 0.97 wt. % Mn at ~60 cm depth. The ratio of Fe/Ti increases and Fe/Mn decreases in the siderite zone (~60 cm depth), due to more efficient Fe and Mn sequestration in the carbonate phase, and not enhanced delivery of Fe or Mn to the system. Ratios are more variable in the upper core, particularly that of Si/Al, precluding clear interpretation of trends (Figure S-1).

In the lower portion of the core (60-90 cm), there are intervals where the Fe_{ox1} pool is increased at the expense of the $Fe(II)_{unsulf}$ pool, potentially indicating a degree of sample oxidation, most likely during collection or storage, which dominantly impacted the most sensitive $Fe(II)_{unsulf}$ phases; these samples are shown in Table S-1, but were removed from the plot shown in the main text.

The concentration of DIC in porewaters was generally at or slightly above the level observed in the deepest ferruginous water mass, with a positive C-isotopic composition consistent with residual DIC reflecting the loss of isotopically light carbon to methane production (Lambrecht *et al.,* 2020).

X-ray Absorption Spectra Supplementary Results and Discussion

Pre-edge Peak Fitting

A baseline was fit to the pre-edge and initial edge jump region of the Fe XANES using a linear and Lorentzian model. Gaussian peaks were fit to the pre-edge peak. Two gaussians produced the best fit for the sediment trap samples. Three gaussians produced the best fit for sediments, although one of the peaks for the 64 and 110 cm samples had a very small area with large relative standard deviation. The centroid energy systematically decreased with depth through the water column and sediments, although the 110 cm sample had a slightly higher energy centroid than the 64 cm sample. Standards with known $Fe^{3+}/\Sigma Fe$ were not analysed with the samples, so a quantitative calibration of $Fe^{3+}/\Sigma Fe$ was not possible. However, the centroid energies are consistent with the sediment trap samples being a mixture of Fe^{2+} and Fe^{3+}, and sediment samples being predominantly Fe^{2+} (Wilke, 2001; Ellison et al., 2020). Pre-edge fit results are reported in Table S-4 and are reported in the Figure S-3.

Linear Combination Fitting

To investigate the composition of the water particulates and sediments in Canyon Lake, linear combination fittings (LCF) of the Fe X-ray adsorption near edge structures (XANES) across 7100 to 7180 eV and extended X-ray adsorption fine structures (EXAFS) across k^3-weighted chi (k)-space 2-8 were performed on the samples using 5 standards (Green Rust Iron, Magnetite, a biogenic Fe (oxyhydr)oxide ["Bio Fe"], Greigite, and Siderite) for the Fe sediment data and 9 standards (Green Rust Iron, Magnetite, Hematite, Lepidocrocite, Bio Fe, Greigite, Siderite, Goethite, and 2-line Ferrihydrite) for the Fe water column particulates. Weighted components were normalized to the total sum, which was not forced to sum to 1, following recommendation by Calvin (2013). However, non-normalized sums were within ± 0.25 from 1. The 'goodness of fit' was determined by R-factors values and the Hamilton Test was utilized as a statistical assessment to indicate the significance between subsequent fits produced from the LCF following parameters outlined by Calvin (2013).

Linear combination fits for the sediment trap material from water column data at 15 m and 20 m had >10 fits that could not be distinguished statistically in normalized energy or in k^3-weighted chi (k)-space. Therefore, this data is excluded from consideration. Sediment trap material from 7.5 m water depth had 2 fits which could not be distinguished in k^3-weighted chi (k)-space and are given in Figure S-4 and Table S-6. Because both fits are equally good, caution should be given to conclusions relying on one fit over the other.

Linear combination fits for the sediment data at 110 cm resulted in one fit that was statistically better than all subsequent fits in normalized energy. For k^3-weighted chi (k)-space, LCF also found one fit that was statistically better than all other fits for sediment data at 22 and 64 cm. The LCF data in normalized energy for 22 and 64 cm and the k^3-weighted chi (k)-space for 110 cm all had between 1-2 additional fits that could not be statistically distinguished and can be seen in Figures S-5 and S-6. A fit that contained Bio Fe, Siderite and Greigite was common across all the samples for the sediment data in both normalized energy and in k^3-weighted chi (k)-space and is shown in Figure S-7. All statistics and values for the LCF results for XANES and EXAFS are given in Table S-5.

Supplementary Tables

Table S-1   Iron phase partitioning data for Canyon Lake Samples. Samples in *italics* displayed indications of oxidation subsequent to core recovery and were not plotted in the main text.

#	Name	Depth (cm)	Fe(II)$_{unsulf}$ (wt.%)	Fe$_{ox1}$(III) (wt.%)	Fe$_{ox2}$ (wt.%)	Fe$_{mag}$ (wt.%)	Fe$_{py}$ (wt.%)	Fe$_{avs}$ (wt.%)	Fe$_{HR}$ (wt.%)	Fe$_{HR}$/ Fe$_T$	Fe$_{py}$/ Fe$_{HR}$	Fe (wt.%) ICP
25	Core C 14 cm	14	2.16	0.30	0.38	0.05	0.23	0	3.12	0.83	0.07	3.75
26	Core C 22 cm	22	2.00	0.33	0.39	0.06	0.18	0	2.96	0.79	0.06	3.74
27	Core C 30 cm	30	2.47	0.19	0.40	0.05	0.24	0	3.34	0.84	0.07	4.00
28	Core C 39 cm	39	2.50	0.19	0.43	0.05	0.22	0	3.39	0.84	0.06	4.06
29	Core C 44 cm	44	2.22	0.17	0.46	0.07	0.16	0	3.09	0.76	0.05	4.06
30	Core C 49 cm	49	2.37	0.25	0.43	0.06	0.19	0	3.30	0.81	0.06	4.06
31	Core C 54 cm	54	2.18	0.42	0.41	0.06	0.18	0	3.24	0.84	0.06	3.86
32	Core C 59 cm	59	1.81	0.58	0.45	0.07	0.16	0	3.07	0.79	0.05	3.90
33	Core C 64 cm	64	2.82	0.82	0.52	0.08	0.18	0	4.42	0.82	0.04	5.41
34	Core C 71 cm	71	2.97	1.22	0.53	0.07	0.15	0	4.95	0.90	0.03	5.47
35	*Core C 78 cm*	*78*	*0.82*	*2.01*	*0.56*	*0.09*	*0.15*	*0*	*3.63*	*0.79*	*0.04*	*4.61*
36	Core C 81 cm	81	2.25	0.74	0.51	0.07	0.16	0	3.74	0.83	0.04	4.50
37	*Core C 84 cm*	*84*	*0.97*	*2.69*	*0.59*	*0.08*	*0.15*	*0*	*4.47*	*0.92*	*0.03*	*4.84*
38	Core C 88 cm	88	2.34	0.72	0.48	0.06	0.20	0	3.79	0.83	0.05	4.58
39	*Core C 94 cm*	*94*	*0.72*	*2.05*	*0.51*	*0.07*	*0.19*	*0*	*3.53*	*0.83*	*0.05*	*4.24*
40	Core C 100 cm	100	2.39	0.52	0.48	0.07	0.19	0	3.66	0.90	0.05	4.06
41	*Core C 105 cm*	*105*	*0.69*	*2.16*	*0.49*	*0.07*	*0.09*	*0*	*3.51*	*0.85*	*0.03*	*4.12*
42	Core C 110 cm	110	2.37	0.32	0.38	0.06	0.20	0	3.33	0.87	0.06	3.82
43	Core C 117 cm	117	2.27	0.65	0.46	0.06	0.22	0	3.66	0.85	0.06	4.29

Table S-2   Siderite saturation calculations (as log Q/K) based on Canyon Lake waters.

Species	Concentration (mg/)	pH	Siderite (log Q/K)
Fe^{2+}	94.330	6	0.185
Fe^{2+}	94.330	6.5	0.9594
Fe^{2+}	94.330	6.8	1.356
Fe^{2+}	94.330	7	1.596
Fe^{2+}	94.330	7.5	2.134
Fe^{2+}	94.330	8	2.598

Table S-3   Initial conditions for siderite saturation calculations based on Canyon Lake bottom water.

Species	Concentration	Units
Al^{3+}	0.363	mg/l
$B(OH)_3$	0.050	mg/l
Ca^{2+}	29.000	mg/l
Cr^{2+}	0.003	mg/l
Fe^{2+}	94.330	mg/l
K^+	1.787	mg/l
Mn^{2+}	3.039	mg/l
Mg^{2+}	7.825	mg/l
Na^+	7.318	mg/l
HPO_4^{2-}	0.232	mg/l
F^-	< 0.1	mg/l
Cl^-	11.300	mg/l
NO_2^-	< 0.1	mg/l
Br^-	0.500	mg/l
SO_4^{2-}	< 0.1	mg/l
NO_3^-	< 0.1	mg/l
HCO_3^-	5.640	mmol/l
O_2	0.041	mg/l
pH	6.8	H^+
Temperature	5.6	C
Siderite	1.225	log Q/K

Table S-4   Fe XANES Pre-Edge Characteristics for Canyon Lake Samples

Sample	Height	Position (eV)	FWHM (eV)	Area	Total Area	Centroid (eV)	χ^2
7.5 m trap	0.024±0.006	7113.03±0.23	2.35±0.21	0.061±0.020	0.147±0.029	7114.08±0.04	2.88x10^{-5}
	0.032±0.005	7114.83±0.20	2.51±0.25	0.086±0.021			
15 m trap	0.025±0.003	7113.76±0.25	3.06±0.28	0.080±0.017	0.104±0.021	7114.06±0.02	1.47x10^{-5}
	0.013±0.005	7115.09±0.04	1.79±0.25	0.024±0.013			
20 m trap	0.032±0.002	7113.42±0.13	2.67±0.17	0.091±0.011	0.127±0.015	7113.88±0.02	2.19x10^{-5}
	0.018±0.004	7115.03±0.09	1.87±0.13	0.036±0.010			
22 cm core	0.024±0.007	7111.84±0.44	2.56±0.41	0.065±0.029	0.148±0.040	7112.72±0.02	1.02x10^{-5}
	0.008±0.011	7112.54±0.14	1.36±0.45	0.012±0.020			
	0.034±0.007	7113.55±0.15	1.98±0.17	0.071±0.018			
64 cm core	0.002±0.001	7110.78±0.09	0.89±0.36	0.002±0.002	0.154±0.131	7112.64±0.01	1.09x10^{-5}
	0.028±0.020	7112.13±1.25	3.02±1.00	0.090±0.094			
	0.026±0.033	7113.44±0.21	2.19±0.46	0.062±0.091			
110 cm core	0.027±0.003	7111.79±0.21	2.50±0.23	0.072±0.015	0.160±0.020	7112.68±0.01	1.04x10^{-5}
	0.005±0.003	7112.54±0.07	1.01±0.24	0.006±0.004			
	0.038±0.005	7113.47±0.08	2.03±0.09	0.082±0.013			

Table S-5 Results of linear combination fitting for **(a)** EXAFS at the Fe K-edge for Canyon Lake sediments and sediment trap material at 7.5 m depth and **(b)** XANES at the Fe K-edge for Canyon Lake sediments. The lowest R factor for multiple fits is the best fit. The *p*-value indicates the significance.

(a) EXAFS

	Green Rust	Bio Fe	Greigite	Siderite	Hematite	R-Factor	*p*-value vs best fit
22cm	-	57.8 ± 4	33.2 ± 5	9.0 ± 1	-	0.0513	-
64 cm	-	49.6 ± 3	30.6 ± 4	19.8 ± 1	-	0.0526	-
110 cm	-	58.8 ± 4	32.5 ± 5	8.7 ± 1	-	0.0630	-
	9.3 ± 3	57.7 ± 6	33.0 ± 7	-	-	0.0842	0.068
	-	91.9 ± 3	-	8.1 ± 2	-	0.0877	0.051
7.5 m		95.4 ± 4	-	15.5 ± 2	15.6 ± 2	0.06636	-
		72.3 ± 6	67.2 ± 8	22.1 ± 2	-	0.07432	-

(b) XANES

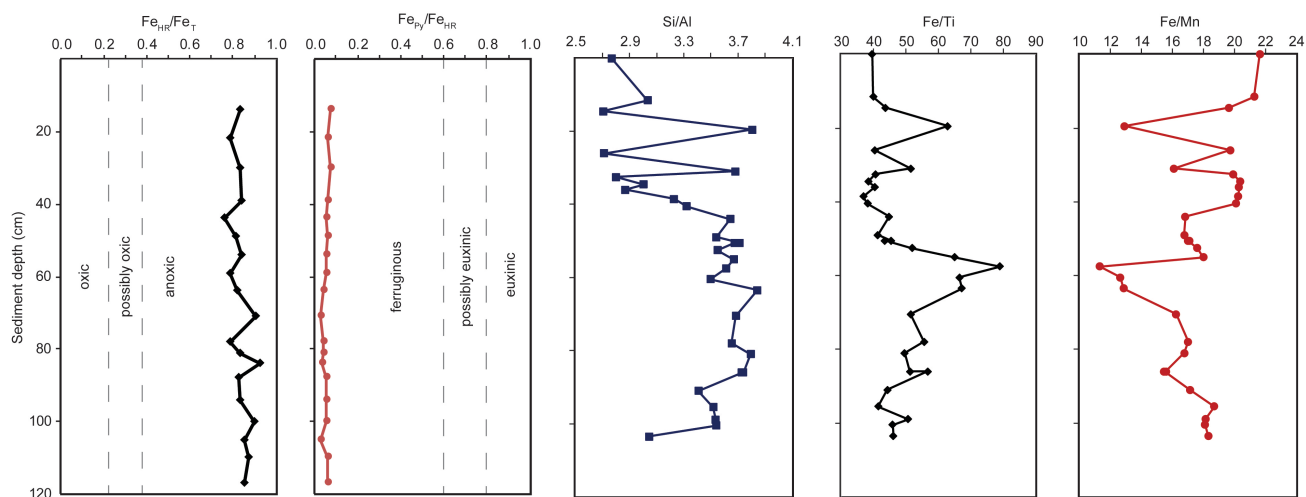|	Green Rust	Magnetite	Bio Fe	Greigite	Siderite	R factor	*p*-value vs best fit
22 cm	36.3 ± 1	-	53.1 ± 0.5	-	10.6 ± 0.7	0.000456	-
	-	-	54.6 ± 0.6	25.2 ± 0.8	20.2 ± 0.5	0.000602	0.087
64 cm	-	-	24.2 ± 0.8	43.7 ± 1	32.1 ± 0.7	0.00117	-
	-	46.4 ± 2	-	24.3 ± 2	29.2 ± 0.7	0.00120	0.59
	27.6 ± 3	49.2 ± 2	-	-	23.2 ± 1	0.00158	0.19
110 cm	-	-	24.2 ± 0.8	43.7 ± 1	32.1 ± 0.7	0.00117	-

Supplementary Figures

Figure S-1   Iron speciation data and selected XRF element ratios for the Canyon Lake core. All speciation samples plot in the anoxic ferruginous field (Poulton and Canfield, 2011). The element ratio of Si/Al implies a consistently low flux of siliciclastic materials to the lake, with perhaps intervals of slight increases (or declines in diatom productivity) in the upper most 40 cm of sediments. The ratio of Fe/Ti implies that the increase in Fe concentration observed in the middle of the core (~60 cm) is not derived from an increased flux of siliciclastic or terrigenous Fe. The decline in the Fe/Mn ratio in the same horizon suggests that the siderite present in that interval preferentially incorporates Fe relative to Mn.
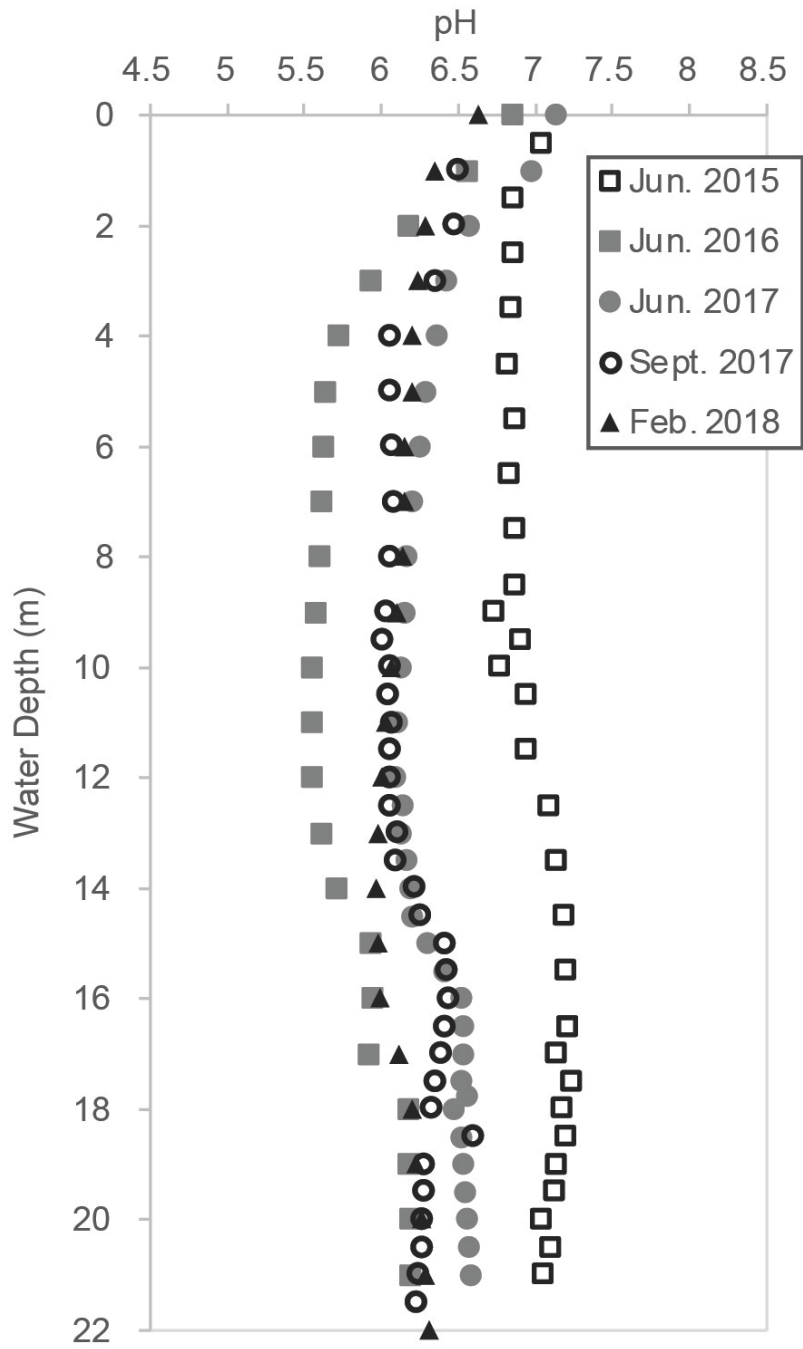
Figure S-2   Canyon Lake pH profiles, 2015-2018. Data from Swanner *et al.* (2021).
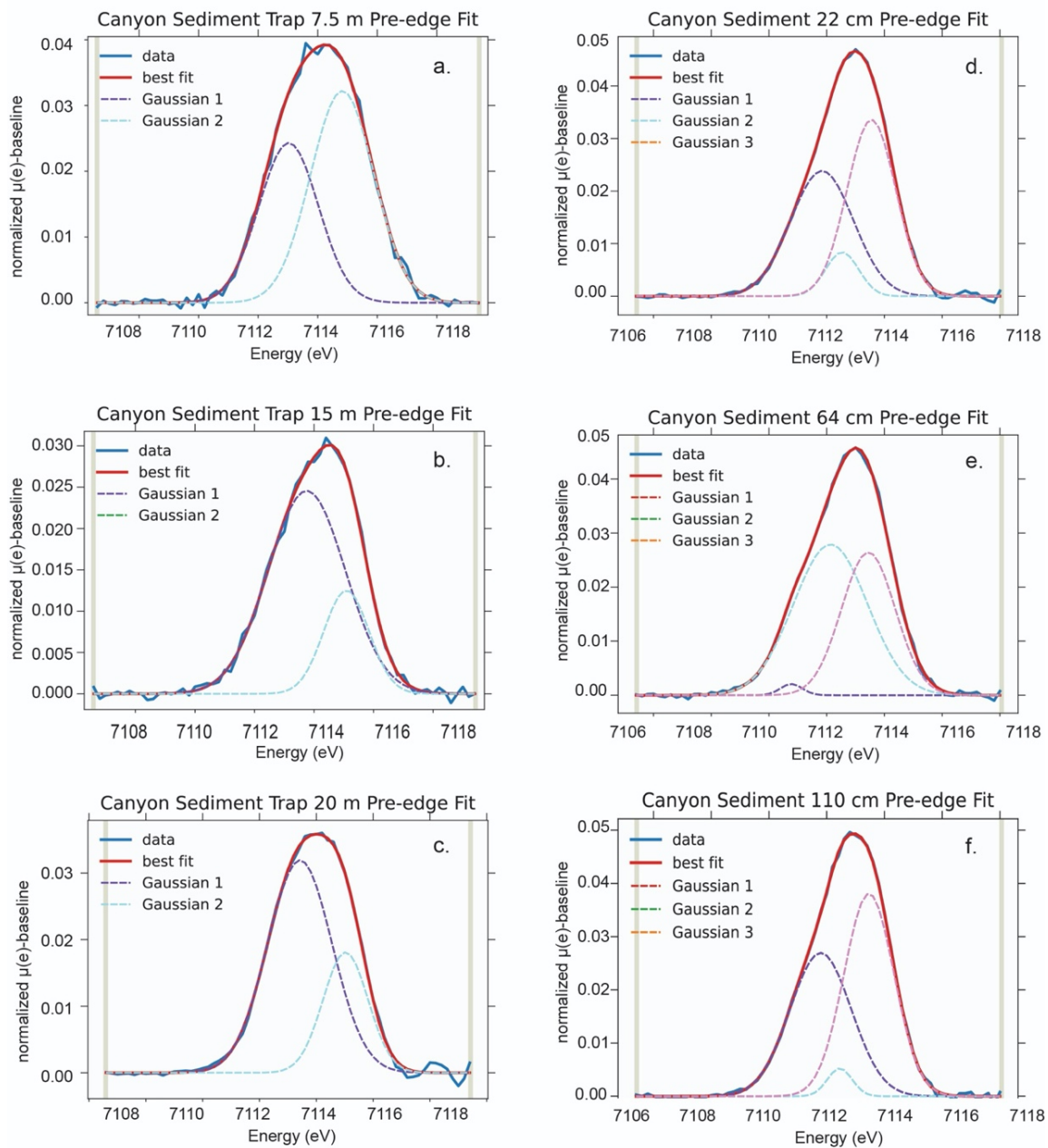
Figure S-3 Baseline subtracted pre-edge fits of sediment trap samples **(a-c)** and sediment samples **(d-f)** from Canyon Lake. The centroid position was 7114.01 ± 0.02 eV for the sediment traps and 7112.68 ± 0.01 eV for sediments.
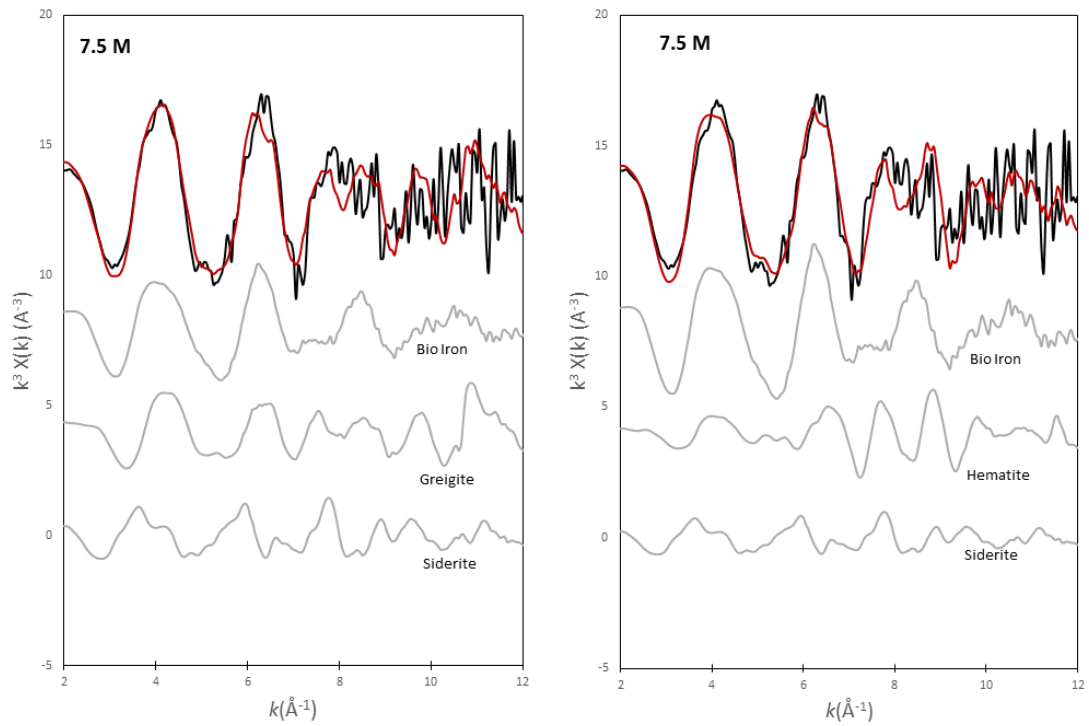
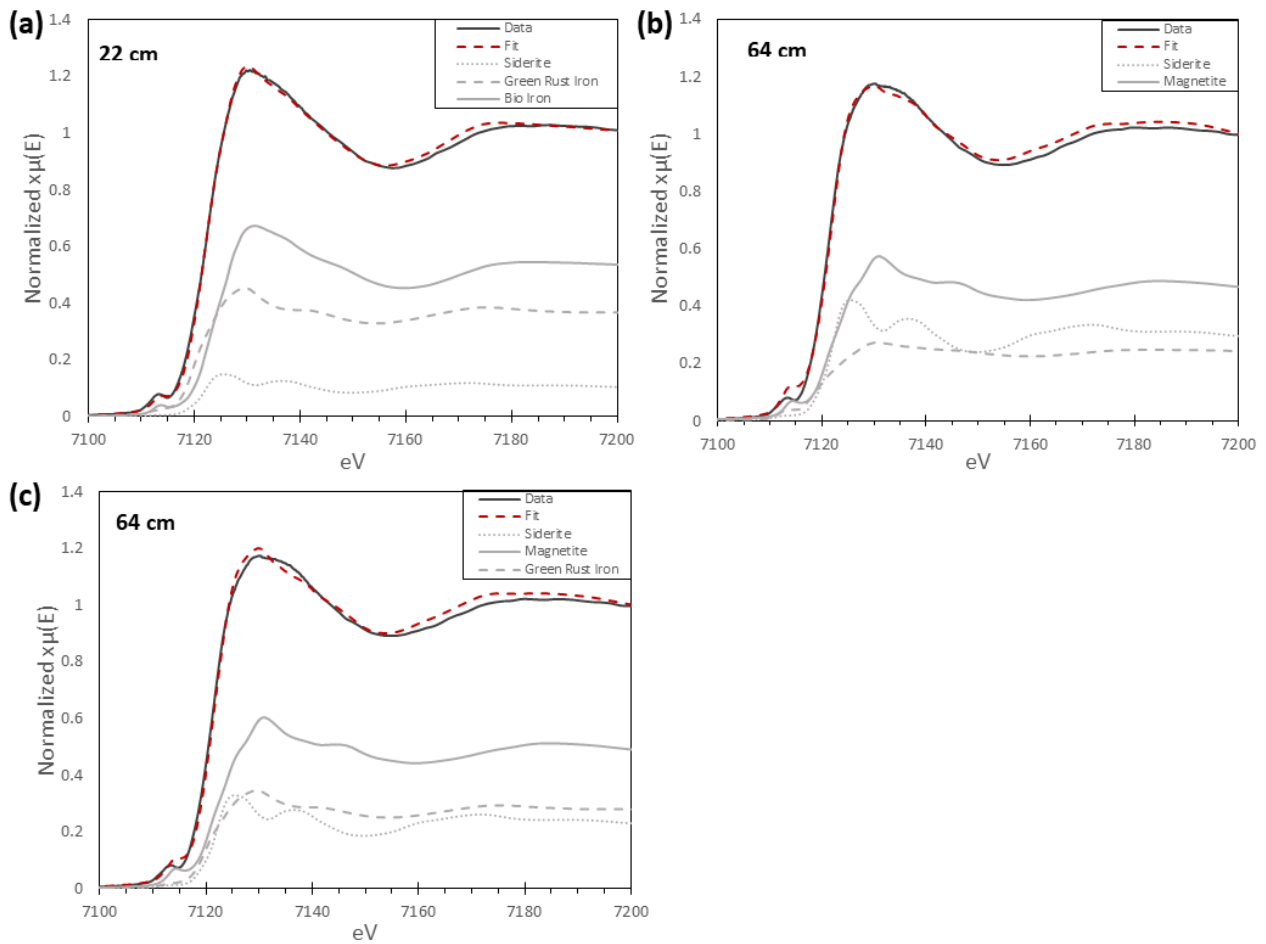**Figure S-4** Linear combination fitting results of the Fe-K edge EXAFS spectra for sediment trap material at 7.5 m water depth. Data for these results are given in Table S-5.

Figure S-5 Linear combination fit results of the normalized XANES Fe K-edge spectra which could not be readily distinguished at sediment depths **(a)** 22 cm and **(b & c)** 64 cm.
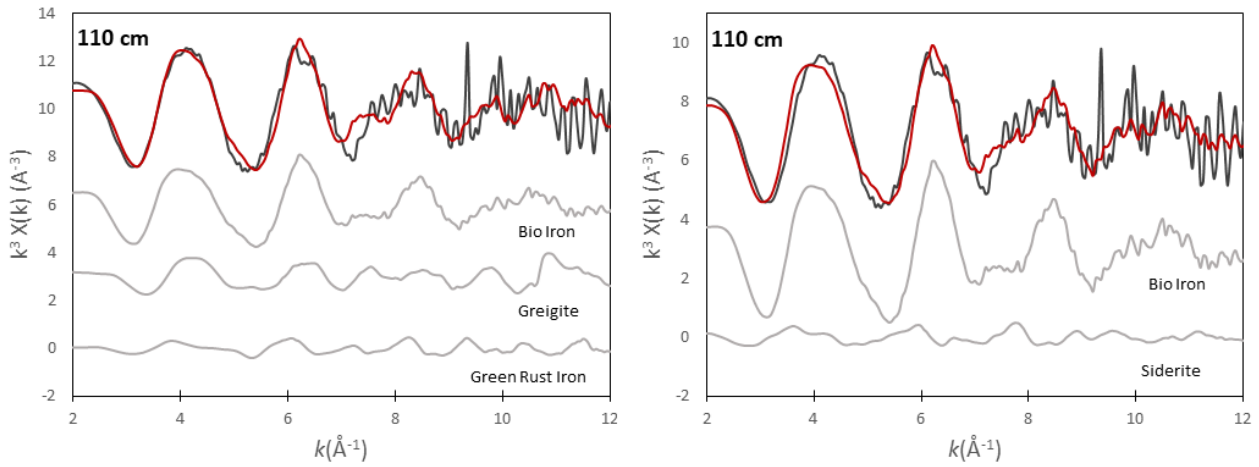
Figure S-6 Linear combination fit results of the Fe K-edge EXAFS spectra which could not be readily distinguished at sediment depth 110 cm.
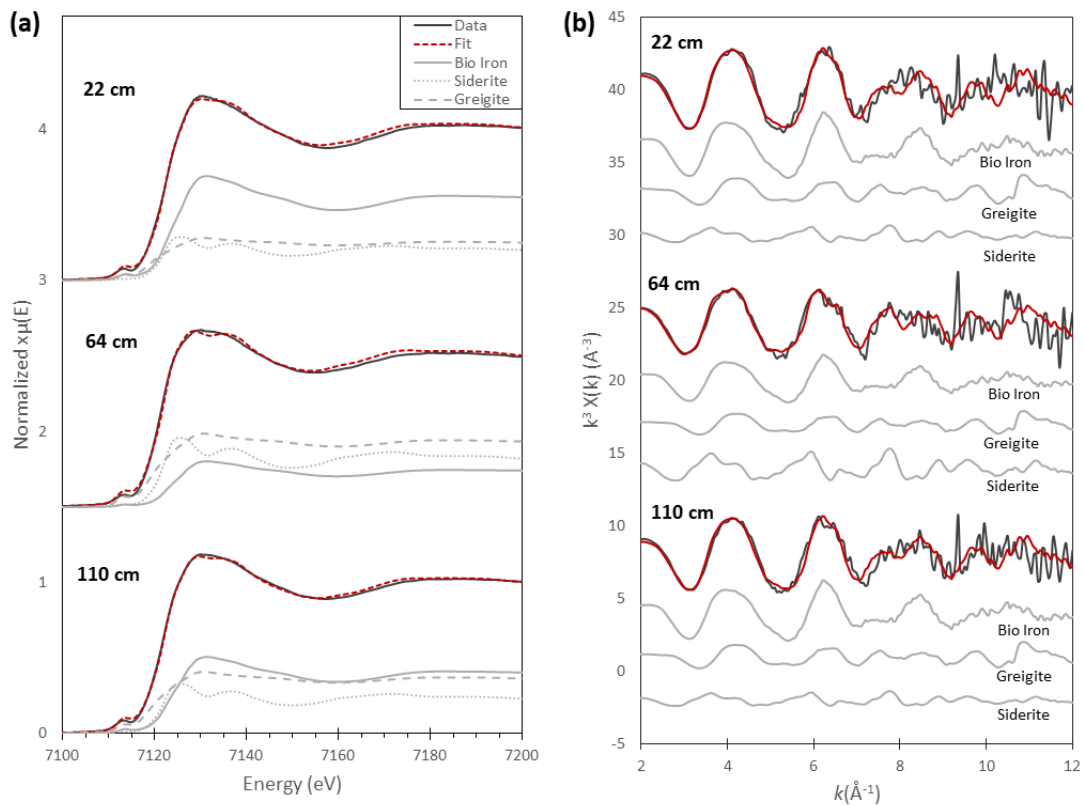

Figure S-7 Linear combination fitting results of the **(a)** Fe K-edge normalized XANES spectra and **(b)** Fe K-edge EXAFS spectra for sediment at 22 cm, 64 cm, and 110 cm depths.

Raw Data including Sample Depths, XRF, XRD, Elementar CS

Attached is our raw data of sample depths, XRF, XRD, and Elementar CS measurements. An Excel version housing all the raw data is available for download from the online version of this article at LINK.

Supplementary Information References

Calvin, S. (2013) Linear Combination Analysis, In: *XAFS for Everyone*, CRC Press, Taylor & Francis Group, Boca Raton, 427.

Canfield D. E., Raiswell R., Westrich J. T., Reaves C. M., and Berner R. A. (1986) The use of   chromium   reduction in the analysis of reduced inorganic sulfur in sediments and shales. *Chemical Geology* 54, 149-155

Ellison, E. T., Mayhew, L.E., Miller, H.M., and Templeton, A. S. (2020) Quantitative microscale Fe redox imaging by multiple energy X-ray fluorescence mapping at the Fe K pre-edge peak. *American Mineralogist* 105, 1812–1829. https://doi.org/10.2138/am-2020-7359

Harris, D., Horwáth, W. R., and Van Kessel, C. (2001) Acid fumigation of soils to remove carbonates prior to total organic carbon or carbon-13 isotopic analysis. *Soil Science Society of America Journal* 65(6), 1853-1856

Islam, R. (2022) Investigating the Formation Mechanisms of Sedimentary Pyrite under Anoxic & Ferruginous Conditions. Iowa State University

Lambrecht, N., Katsev, S., Wittkop, C., Hall, S. J., Sheilk, C.S., Picarad, A., Fakhraee, M., and Swanner, E. D. (2020) Biogeochemical and physical controls on methane fluxes from two ferruginous meromictic lakes. *Geobiology*, https://doi.org/10.1111/gbi.12365

Lambrecht, N., Wittkop, C., Katsev, S., Fakhraee, M., and Swanner, E. D. (2018) Geochemical Characterization of Two Ferruginous Meromictic Lakes in the Upper Midwest, USA. *Journal of Geophysical Research: Biogeosciences,* p.1-16

Ledesma, G., Islam, R., and Swanner, E. D. (2023) Evaluation of preservation protocols for oxygen-sensitive minerals within laminated aquatic sediments. *Limnology and Oceanography Methods.* https://doi.org/10.1002/lom3.10533

Meyers, P.A., and Ishiwatari. R. (1993) Lacustrine organic geochemistry—an overview of indicators of organic matter sources and diagenesis in lake sediments. *Organic Geochemistry* 20, 867-900.

Poulton S.W. (2021) The Iron Speciation Paleoredox Proxy (Elements in Geochemical Tracers in Earth System Science), *Cambridge University Press.* https://doi.org/10.1017/9781108847148

Poulton S. W., and Canfield D. E. (2005) Development of a sequential extraction procedure for iron: implications for iron partitioning in continentally derived particulates. *ChemicalGeology 214,* 209-221

Poulton S. W., and Canfield D. E. (2011) Ferruginous conditions: A dominant feature of the ocean through Earth's history. *Elements* 7, 107-112

Stookey L. L. (1970) Ferrozine-A new spectrophotometric reagent for iron. *Analytical Chemistry* 42, 779-781

Swanner, E.D., Lambrecht, N., Wittkop, C., Katsev, S., Ledesma,G., and Leung, T. (2021) Water properties of Brownie Lake, MN and Canyon Lake, MI from 2015-2019. *Environmental Data Initiative.* https://doi.org/10.6073/PASTA/4EAF698B4EFBAF793B83D95F464D1672

Webb, S. M. (2005) SIXpack: a graphical user interface for XAS analysis using IFEFFIT. *Physica Scripta.* https://doi.org/10.1238/Physica.Topical.115a01011

Wilke, M. (2001) Oxidation state and coordination of Fe in minerals: An Fe K-XANES spectroscopic study. *American Mineralogist* 86, 714. https://doi.org/10.2138/am-2001-5-612

Wright, H.E., Jr. (1980) Coring of soft lake sediments. *Boreas* 9, 104-114.

Xiong Y., Guilbaud R., Peacock C. L., Cox R. P., Canfield D. E., Krom M. D., and Poulton S.W. (2019) Phosphorus cycling in Lake Cadagno, Switzerland: A low sulfate euxinic ocean analogue. *Geochimica et Cosmochimica Acta* 251, 116-135

Zegeye A., Bonneville S., Benning L. G., Sturm A., Fowle D. A., Jones C., Canfield D. E., Ruby C., MacLean L. C., Nomosatryo S., Crowe S. A., and Poulton S. W. (2012) Green rust formation controls nutrient availability in a ferruginous water column. *Geology* 40, 599-602